

Bottom and top reconstruction as benchmarks for the ILD Detector

M.S. Amjad^a, A. Irlles^b, V. Lohezic^c, Y. Okugawa^d, R. Pöschl^b, F. Richard^b,
H. Yamamoto^d, R. Yonamine^d

^aCOMSATS Institute of Information Technology, Islamabad, Pakistan

^bLaboratoire de l'Accélérateur Linéaire, CNRS/IN2P3 et Université de Paris-Sud, Centre Scientifique d'Orsay
Bâtiment 200, BP 34, 91898 Orsay CEDEX, France

^cUniversité Paris-Sud, 15 Rue Georges Clemenceau, 91400 Orsay, France

^dTohoku University, 6-3 Aoba Aramaki-aza Aoba-ku, Sendai 980-8578, Japan

Abstract

A comprehensive study of bottom-quark pair and top-quark pair production using the semi-leptonic decay channel at $\sqrt{s} = 500$ GeV is presented that benchmark the performance of the current so-called *large* and *small* models of the ILD Detector. The event reconstruction exploits distinguished features of the detector such as lepton identification, vertex charge reconstruction and particle ID with the central TPC of the ILD Detector. With these techniques the final state leptons, the b -quark and \bar{b} -quark and the W can be unambiguously reconstructed. Both detector models perform similarly well with a slight advantage of the large detector model. In case of top quark pair production the selection efficiency is between 30% and 60% for semi-leptonic events. For this channel the note presents an update of the perspective of the physics potential w.r.t. earlier studies for an integrated luminosity of 3200 fb^{-1} . The results for $e^+e^- \rightarrow b\bar{b}$ demonstrate that also this channel can accurately measured at $\sqrt{s} = 500$ GeV.

1. Introduction

Heavy quarks may be messengers of new physics of primary importance [1]. Their large mass compared with other fermions can be explained in Randall Sundrum models [2, 3] featuring warped extra dimensions that are dual to model, which assume that the heavy quarks are composite objects [4]. High precision e^+e^- collisions with polarised beams around the TeV scale are ideally suited to detect new physics effects [5, 6]. Precise measurements of the electroweak couplings of third-generation quarks require superb detector performance in terms of flavour tagging including the event by event determination of the charge of the final state jets to avoid for example migrations in polar angle spectra and/or to reconstruct events in which the heavy quark charge is the only handle to distinguish between particles and anti-particles. The charge determination happens mainly by a combination of the determination of the summed charge of tracks pointing to a secondary vertex or by the identification of the charge of a final state Kaon. This in turn requires a successful particle identification by the detector. Therefore processes with heavy quark final states, i.e. $e^+e^- \rightarrow \phi b\bar{b}$ and $e^+e^- \rightarrow t\bar{t}$ are highly relevant for the benchmarking of the detector performance. In short one can test the following detector capacities.

- Track finding efficiency
- Stringent test of (secondary) vertexing
- Particle ID

In case of $e^+e^- \rightarrow t\bar{t}$ leptonic and semi-leptonic decays of the t -quark pair provide an important additional handle for the accurate measurement of the final state. The analysis presented in this

41 note focuses on the semi-leptonic decay mode of the top-quark pair. The analysis of $t\bar{t}$ production
 42 and $b\bar{b}$ production share a number of commonalities. Therefore these two analyses are joined in this
 43 note. The analyses presented in this note start out from the PhD thesis of Sviatoslav Bilokin that are
 44 based on the DBD samples and software versions [7]. This work has in part been published in Ref [6].
 45 The analyses are ported to the large, IDR-L, and small, IDR-S, detector models, respectively, of the
 46 ILD detector [8] for the International Linear Collider [9]. The research program includes high-statistics
 47 running at $\sqrt{s} = 250$ GeV and $\sqrt{s} = 500$ GeV. For further details of the operation scenarios see Ref. [10].
 48 For the process $e^+e^- \rightarrow b\bar{b}$ an analysis at $\sqrt{s} = 500$ GeV is presented instead of $\sqrt{s} = 250$ GeV as
 49 in Ref. [6]. The results here benefit from a refined analysis strategy for the ILD paper that is under
 50 review in ILD.

51 2. Methods, tools and Monte Carlo samples

52 For the event reconstruction we use the `ILCSOFT` version `v02-00-02`. The software allows for a full
 53 detector simulation and event reconstruction including digitisation steps. For the analyses presented
 54 we use the versions `ILD_s5_o1_v02` and `ILD_15_o1_v02` of the detector model.

55 For the event reconstruction we use the following methods

- 56 • ‘Core tools’

- 57 – In case of $e^+e^- \rightarrow t\bar{t}$ we use the standard Durham algorithm for jet clustering (`ee_genkt_algorithm`
 58 in internal nomenclature) and the Valencia algorithm for $\gamma\gamma$ background removal. Both al-
 59 gorithms are implemented in the `FastJet` package.
- 60 – In case of $e^+e^- \rightarrow b\bar{b}$ we use the Valencia jet algorithm implemented in `LCFIPlus` (`ValenciaVertex`
 61 in internal nomenclature). We apply the option in which the algorithm does not break sec-
 62 ondary vertices. In this algorithm the distance between two objects is calculated as

$$d_{ij} = 2 \min(E_i^{2\beta}, E_j^{2\beta})(1 - \cos \theta_{ij})/R^2 \quad (1)$$

63 The distance of a particle i to the beam is calculated according to.

$$d_{iB} = E^{2\beta} \sin^{2\gamma} \theta_{iB} \quad (2)$$

64 The jet algorithm is run with the following settings: $\alpha = \beta = \gamma = 1$, $R = 1.4$

- 65 – We use the `LeptonFinder` to identify isolated electrons and muons in semi-leptonic $t\bar{t}$ events.
- 66 – For the vertex finding we use the `LCFIPlus` in a private version maintained by Ryo. This
 67 version will soon be implemented into the official `ILCSOFT` package.

- 69 • Tools developed for the study

- 70 – The `VertexRestorer` Processor identifies reconstructed tracks that have not been associated
 71 to secondary vertices from B-Meson decays but belongs to this decay according to the
 72 Monte Carlo Truth information. It then recovers the ‘lost’ tracks by means of the impact
 73 parameters d_0 (transversal) and z_0 (longitudinal). In this present note the recovery uses
 74 only the impact parameter d_0 since the algorithms needs to be adapted for the vertex
 75 smearing present in the simulation for the IDR.
- 76 – The `ParticleTagger` Processor identifies the Kaons by means of the dE/dx measured
 77 in the TPC of ILD. It selects a strip in the dE/dx -momentum plane with a high kaon
 78 concentration. The efficiency and the purity of the Kaon selection vary as a function of the
 79 width of this strip.

- 80 – The `QQbarAnalysis` Processor calculates the jet charge and the polar angle of the bottom
81 and top quark pair, respectively. It contains separate methods for the bottom and top quark
82 pair analysis.
- 83 – The `TrashRecoProcessor` enables comparisons between reconstructed and generated quan-
84 tities.
- 85 – The described tools are available under <https://github.com/qqbaranalysis>. This repository
86 contains also a set of macros necessary for the final steps of the analysis.
- 87 • The following method combines the results of the two (nearly independent) charge measurements
88 on the b and \bar{b} jet into a robust charge determination.

$$\left. \begin{aligned} N_{acc} &= Np^2 + Nq^2 \\ N_{rej} &= 2Npq \\ 1 &= p + q \end{aligned} \right\} N_{corr} = N_{acc} \cdot \frac{p^2}{p^2 + q^2} \quad (3)$$

89 where N is total number of events, N_{acc} and N_{rej} are the number of events that were accepted
90 and rejected, respectively. The p and q values represent the probabilities for a correct or an
91 incorrect reconstruction of the b -quark charge, respectively. Solving this equation allows to
92 correct for migrations caused by imperfect reconstruction or $B^0 - \bar{B}^0$ oscillations in the resulting
93 polar angle spectrum. The correction has been applied to the $b\bar{b}$ studies but not (yet) for $t\bar{t}$.
94 For the latter the selection scheme in $t\bar{t}$ is more involved rendering its application less straight
95 forward since e.g. the b -quarks are not necessarily back-to-back.

96 2.1. Monte Carlo samples

97 Samples generated with WHIZARD 1.95. Top quark pair production is the dominant process in
98 the $e^+e^- \rightarrow b\bar{b}l\nu q\bar{q}$ sample, but it contains also single t and WWZ . In case of the t quark study we
99 have analysed samples for the beam polarisations $\mathcal{P}_{e^-}, \mathcal{P}_{e^+} = \pm 1, \mp 1$. In case of the b quark study we
100 have studied only the configuration $\mathcal{P}_{e^-}, \mathcal{P}_{e^+} = \mp 1$ since this study is just considered as a supporting
101 study for the t quark analysis and the chosen polarisation configuration is the more challenging for the
102 detector performance due to larger migration effects in the polar angle reconstruction.

103 More precisely the results presented in this note are based on the following samples:

- 104 • $e^+e^- \rightarrow t\bar{t}$:
 - 105 – $yyxye\nu, \mathcal{P}_{e^-}, \mathcal{P}_{e^+} = \mp 1$: <https://ild.ngt.ndu.ac.jp/elog/opt-data/?GenProcessID=108670>
106 This sample contains the final state resulting from the $W \rightarrow e\nu$ decay.
 - 107 – $yyxye\nu, \mathcal{P}_{e^-}, \mathcal{P}_{e^+} = \pm 1$: <https://ild.ngt.ndu.ac.jp/elog/opt-data/?GenProcessID=108670>
108 This sample contains the final state resulting from the $W \rightarrow e\nu$ decay.
 - 109 – $yyxy\nu, \mathcal{P}_{e^-}, \mathcal{P}_{e^+} = \mp 1$: <https://ild.ngt.ndu.ac.jp/elog/opt-data/?GenProcessID=108675>
110 This sample contains the final state resulting from the $W \rightarrow \ell\nu$ decay with $\ell = \mu, \tau$. For
111 the analysis presented here the final state with $\ell = \tau$ has been discarded.
 - 112 – $yyxy\nu, \mathcal{P}_{e^-}, \mathcal{P}_{e^+} = \pm 1$: <https://ild.ngt.ndu.ac.jp/elog/opt-data/?GenProcessID=108676>
113 This sample contains the final state resulting from the $W \rightarrow \ell\nu$ decay with $\ell = \mu, \tau$. For
114 the analysis presented here the final state with $\ell = \tau$ has been discarded.
 - 115 – $yyxy\nu, \mathcal{P}_{e^-}, \mathcal{P}_{e^+} = \pm 1$: <https://ild.ngt.ndu.ac.jp/elog/opt-data/?GenProcessID=108676>
116 This sample contains the final state resulting from the $W \rightarrow \ell\nu$ decay with $\ell = \mu, \tau$. For
117 the analysis presented here the final state with $\ell = \tau$ has been discarded.
 - 118

- 119 • $e^+e^- \rightarrow b\bar{b}$: The $b\bar{b}$ events are extracted from a sample of simulated $q\bar{q}$ events <https://ild.ngt.ndu.ac.jp/eelog/opt-data/?GenProcessID=250114> with $q = u, d, s, c, b$. The generated cross section for these events is 32470 fb and the total integrated luminosity is about 46 fb^{-1} . The genuine $e^+e^- \rightarrow b\bar{b}$ at 500 GeV is about 4% of the total cross section yielding a total number of events of about 60000.

124 Note that the analysis of the $e_R^+e_L^- \rightarrow t\bar{t}$ came quite late in the study since it is generally considered
 125 that similar to $e^+e^- \rightarrow b\bar{b}$ the $e_L^+e_R^- \rightarrow t\bar{t}$ is the more challenging channel. Therefore, the corresponding
 126 control plots in Secs. 3 and 4.2 are only given for this channel in this note.

127 3. Efficiencies and Control plots

128 Figure 1 demonstrates that the studies presented in this note test the detector performance for
 129 very different momenta of the final state b quark.

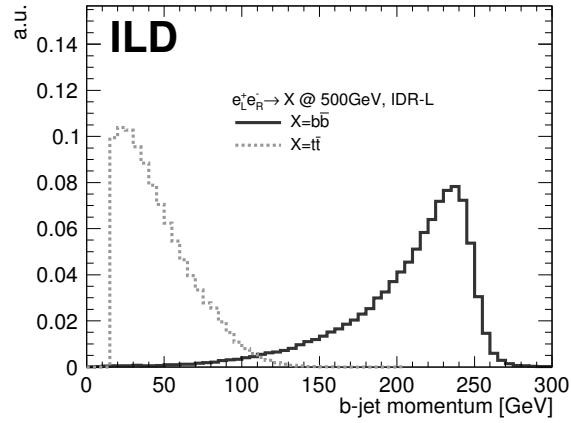


Figure 1: Momentum of the b -jet with cheated identification for $e^+e^- \rightarrow b\bar{b}$ and $e^+e^- \rightarrow t\bar{t}$ processes.

130 The Figs. 2 and 3 show the missed tracks before and after vertex recovery for the $e^+e^- \rightarrow b\bar{b}$ and
 131 $e^+e^- \rightarrow t\bar{t}$ analyses, respectively. Both figures suggest a systematic improvement in the assignment of
 132 secondary vertices.

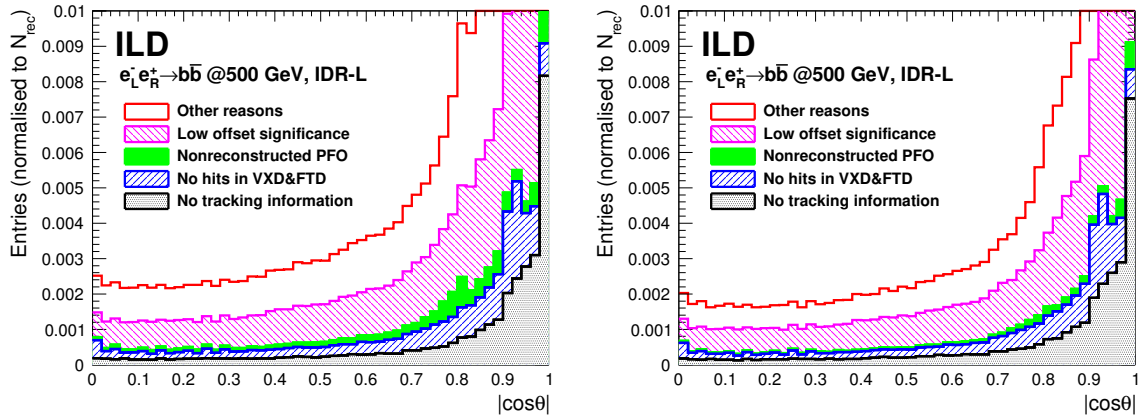


Figure 2: Polar angle of missed tracks before (left) and after (right) vertex recovery in case of the $e^+e^- \rightarrow b\bar{b}$ process.

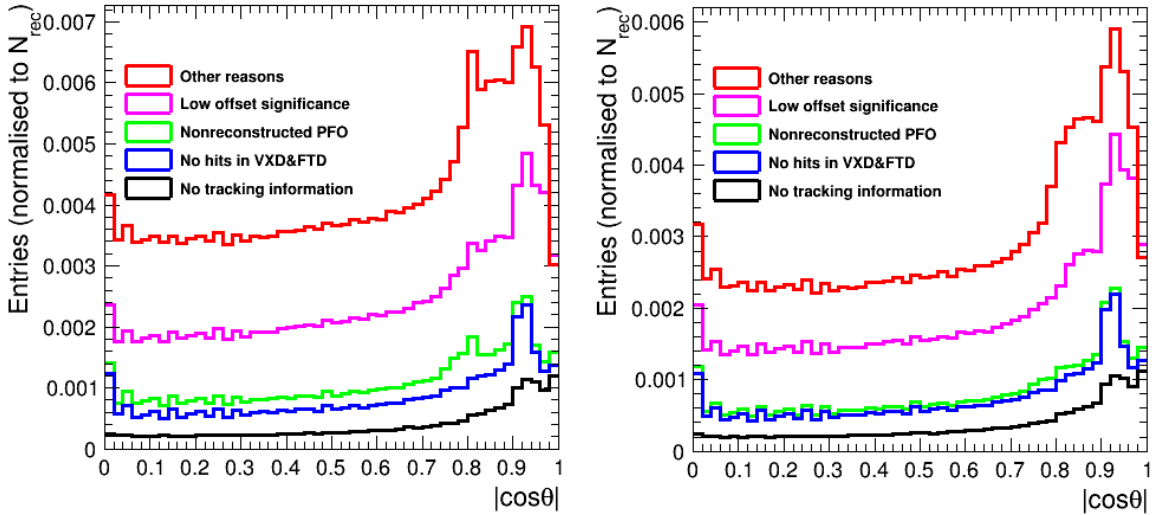


Figure 3: Polar angle of missed tracks before (left) and after (right) vertex recovery in case of the $e^+e^- \rightarrow t\bar{t}$ process.

133 This improvement is quantified in Figs. 4 and 5 where the purity of the b -charge reconstruction
 134 is shown as a function of the b -tag value, the reconstructed b -momentum $|p_{had}|$ the number of
 135 reconstructed tracks assigned to a secondary vertex N_{rec} and finally the polar angle of the b -hadron.
 136 here denoted as $|\cos\theta|$. The b -charge purity is defined as

$$p_b = N_{correct}/N_{jet,tot}. \quad (4)$$

137 with $N_{correct}$ being the number of b -jets with correctly reconstructed b quark charge. This value nor-
 138 malised to the total number of b -jets $N_{b-jet,tot}$ for which a charge assignment according to e.g. Table 2
 139 can be made.

140 The improvement is larger for the process $e^+e^- \rightarrow t\bar{t}$ than for $e^+e^- \rightarrow b\bar{b}$. Qualitatively this is
 141 expected since as a consequence of the different b -jet momenta, see Fig. 1, also the tracks produced
 142 in the decay of the b -hadron are softer in case of top-pair production. In case of $e^+e^- \rightarrow t\bar{t}$ the
 143 improvement is 10% over a large range in $|\cos\theta|$ and mainly driven by three to five prong decays.
 144 Both results will further improve once the vertex recovery takes also the impact parameter z_0 into
 145 account. All results shown so far in this section have been obtained for the large detector model. The
 146 conclusions for the small detector model are similar.

147 The lower right panels of Figs. 4 and 5 show a drop in purity for large values of $|\cos\theta|$. This is
 148 compatible with the drop in acceptance that is shown in Fig. 6 for the case $e^+e^- \rightarrow b\bar{b}$ as a function
 149 of the polar angle of the reconstructed b -jet $|\cos\theta_b|$. Within statistical errors the results are the same
 150 for the large and the small detector model. However, towards large values of $|\cos\theta_b|$ the large detector
 151 performs systematically better than the small detector.

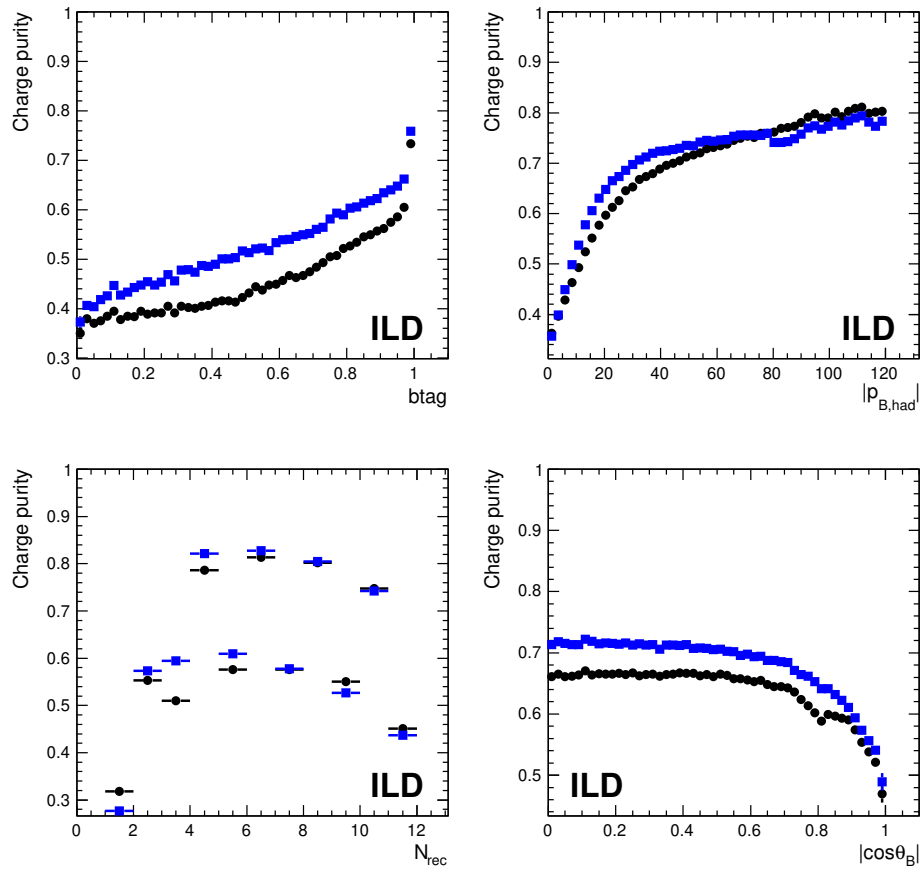


Figure 4: Purity before and after vertex recovery in case of the $e^+e^- \rightarrow t\bar{t}$ process for different observables.

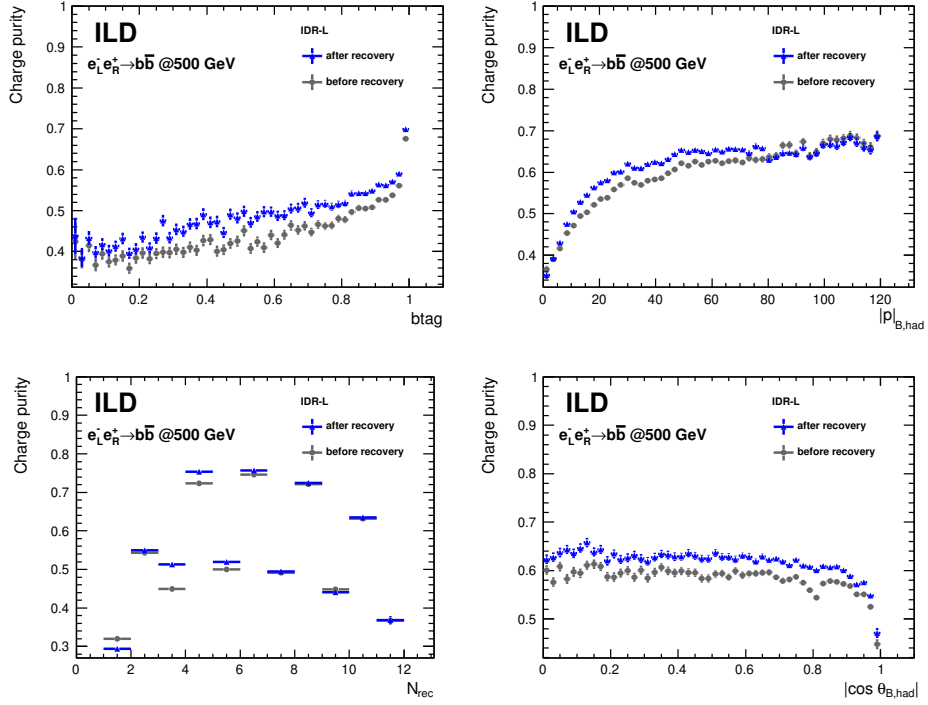


Figure 5: Purity before and after vertex recovery in case of the $e^+e^- \rightarrow t\bar{t}$ process for different observables.

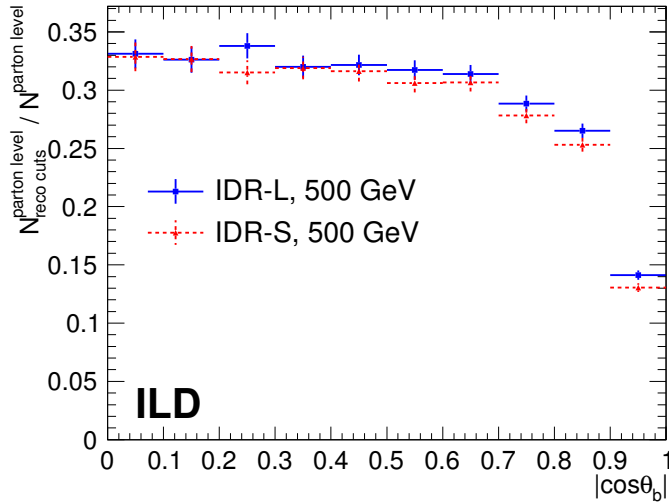


Figure 6: Detector acceptance distribution for b-tagged jets. Note the figure shows the acceptance after the full selection given in Tab. 1.

152 A component that distinguishes the ILD Detector from other proposals for e^+e^- colliders is the TPC
 153 as the central tracking system. Beside the precise momentum measurement the dE/dx measurement
 154 in the gaseous medium allows for a particle identification. Since around 87% of B-Mesons (neutral or
 155 charged) contain a charged Kaon among their decay products the particle ID can support greatly the

156 charge determination of the b quark.

157 The left part of Fig. 7 shows the dE/dx values obtained in simulation for different particle types
 158 as a function of the particle momentum. The lines indicate a strip with an accumulation of signals
 159 produced by Kaons. A minimum momentum of 2 GeV is required for the selection of Kaons. The
 160 right part of Fig. 7 shows the variation of the purity as a function of the Kaon selection efficiency
 161 that corresponds to a variation of the width of the strip in the previous figure. A closer look into the
 162 separation power in different momentum ranges is given in App. A.

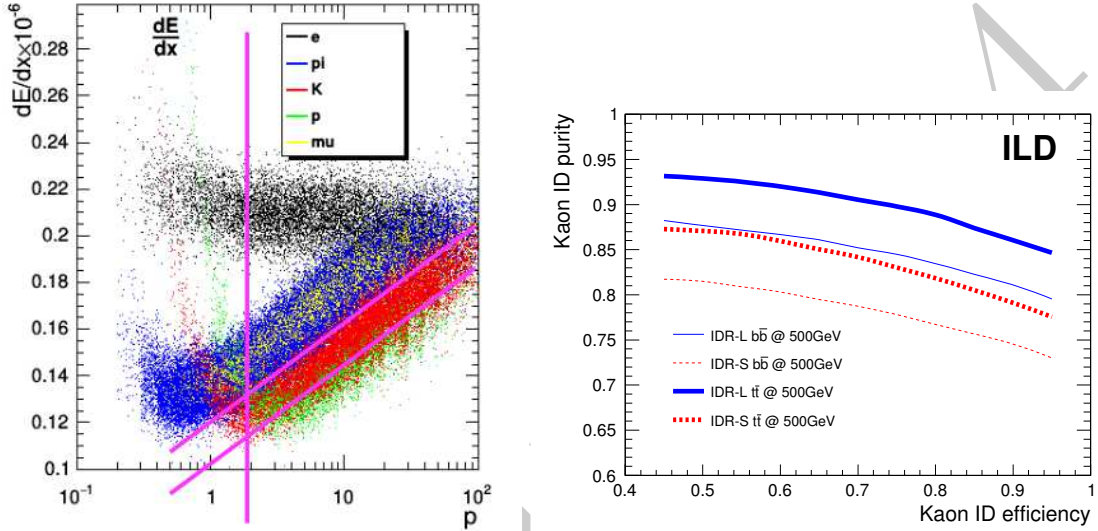


Figure 7: Left: Simulated dE/dx spectrum for different particle types. The lines indicate the cuts for the Kaon selection. Right: Purity of the Kaon selection as a function of the Kaon selection efficiency.

163 4. Event selection

164 In the following the event selection of the two final states under study will be presented. The
 165 different complexities of the final states require different set of cuts. The t quark is composed from its
 166 decay products, the b quark and the W boson and the final state le

167 4.1. Analysis details specific to the $e_L^- e_R^+ \rightarrow b\bar{b}$ analysis

168 Table 1 shows the selection efficiencies for the $e_L^- e_R^+ \rightarrow b\bar{b}$ analysis. In this case events that are
 169 subject to the radiative return to the Z , implying an energetic final state photon, have to be suppressed.
 170 Therefore cuts on the sum of the masses of the two jets and a cut on the photon energy are introduced.
 171 The overall efficiency after selection of events with consistent b quark charge is with around 28% to
 172 29% similar for both detector models. For the b -charge measurement opposite charges in opposite jets
 173 are required. The charges are either derived from the tracks pointing to the secondary vertex or from
 174 the Kaon charge or from a combination of both. An event is selected if there is one combination with
 175 a consistent result. The efficiencies for the different methods are given in Tab. 2. The purity of the
 176 different methods is shown in Fig. 8. In both cases there is no large difference between the two detector
 177 models although the large detector seems to perform slightly better for the double Kaon method. This
 178 suggests that the smaller outer radius of the TPC puts a, however minor, on the dE/dx measurement.

179

$e_L^- e_R^+ \rightarrow b\bar{b}$ at 500 GeV

	IDR-L			IDR-S		
	Signal	B _{q\bar{q}} /S	B _{rad.Z} /S	Signal	B _{q\bar{q}} /S	B _{rad.Z} /S
Full sample	100.0%	1800.5%	359.1%	100.0%	1800.6%	359.0%
$b_{tag}(jet_1) > 0.9$ and $b_{tag}(jet_2) > 0.2$	70.2%	2.3%	147.7%	69.9%	2.3%	149.0%
$m_{jet_1+jet_2} > 200 GeV$	68.2%	1.4%	6.7%	67.8%	1.2%	6.7%
$E_{photon} < 100 GeV$	64.8%	1.3%	1.7%	64.3%	1.2%	1.6%
double jet-charge measurement	28.9%	1.0%	1.0%	27.9%	0.9%	1.0%

Table 1: Selection efficiency and B/S rejection for some bkg sources

$e_L^- e_R^+ \rightarrow b\bar{b}$ at 500 GeV

	IDR-L	IDR-S
$Vtx+Vtx$	12.9%	12.8%
$K+K$	4.4%	4.0%
$Vtx+K$ (diff. jets)	3.9%	3.7%
$Vtx+K$ (same jet)	7.7%	7.4%

Table 2: Final selection efficiency, after double jet-charge measurement

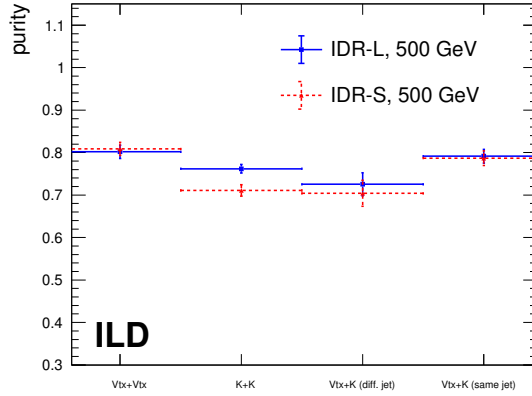


Figure 8: Purity of the methods listed in Tab. 2 used for the reconstruction of the vertex charge in the $e_L^- e_R^+ \rightarrow b\bar{b}$.

180 *4.2. Analysis details specific to the $e^+e^- \rightarrow t\bar{t}$ analysis*

181 The t quark is composed from its decay products, the b quark and the W boson and the charge of
 182 the lepton is a measure to distinguish the t from the \bar{t} quark.

183 Figure 9 shows in the left panel the energy distribution of the isolated lepton in the laboratory
 184 frame. The distribution features a maximum at around 30 GeV and a tail towards higher energies. The
 185 right panel shows the polar angle spectrum of the isolated lepton. The distribution decreases slightly
 186 with a sharp drop at the acceptance limit of the detector. The distribution reveals also acceptance
 187 drops at $\cos\theta_\ell = 0$ and $\cos\theta_\ell = 0.8$ that correspond to the position of the TPC anode plate and the
 188 barrel-endcap transition region, respectively.

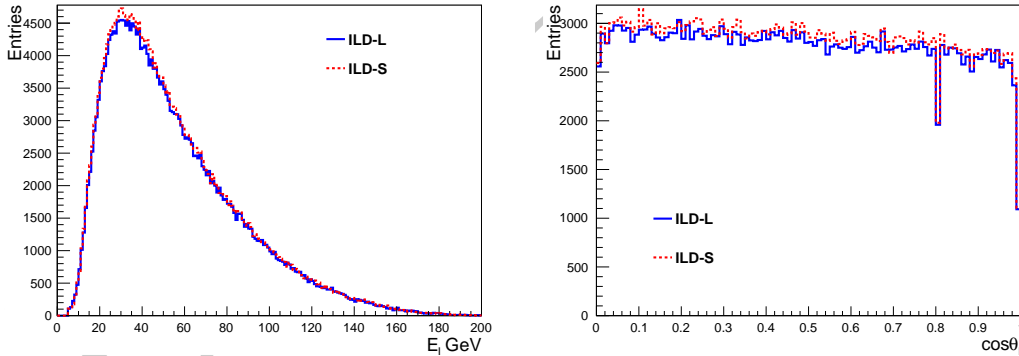


Figure 9: Left: Energy of the isolated lepton in $e_L^+ + e_R^- \rightarrow t\bar{t}$. Right: Polar angle distribution of the isolated lepton in $e_L^+ e_R^- \rightarrow t\bar{t}$.

189 For completeness Fig, 10 shows the mass distribution of the hadronic W and the hadronic t quark.

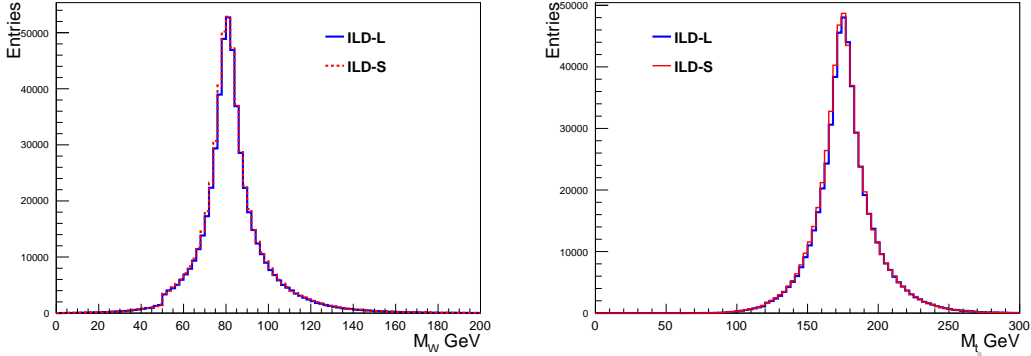


Figure 10: Left: Mass distribution of the hadronic W in $e_L^+ e_R^- \rightarrow t\bar{t}$. Right: Mass distribution of the hadronic t quark in $e_L^+ e_R^- \rightarrow t\bar{t}$.

190 Tables 3 and 5 give the efficiencies after each cut applied for the selection of $t\bar{t}$ events. The first
 191 part lists *General selection cuts* that were already used in Ref. [5].

192 The polar angle of the t quark $\cos\theta_t$ is reconstructed from the hadronically decaying t quark. For
 193 the polar angle spectrum the charge of the t quark has to be determined and the b quark and the
 194 W -boson have to be correctly associated. This is more involved in the $e_L^- e_R^+ \rightarrow t\bar{t}$ case than in the
 195 $e_R^- e_L^+ \rightarrow t\bar{t}$ case due to the different kinematics provoked by the $V - A$ interaction of the t quark
 196 decay. The different steps for an accurate reconstruction of the polar angle spectrum are listed in the
 197 following¹.

- 198 • In a first step further cuts on the sum of the Lorentz factor of the two tops of $\gamma_t^{had} + \gamma_t^\ell > 2.4$
 199 is applied. Here γ_t^{had} is the Lorentz factor of the hadronically decaying t quark and γ_t^ℓ the
 200 Lorentz factor of the leptonically decaying t quark. In case of $e_L^- e_R^+ \rightarrow t\bar{t}$ a cut on the B -hadron
 201 momentum of $p_{B,had.} > 15$ GeV is applied in addition.
- 202 • The semi-leptonic decay of the t quark gives powerful information for the event reconstruction
 203 giving rise to the variable L_{cut} , which means the charge of the isolated lepton plus a cut on the
 204 event quality of $\chi^2 < 15$ that is motivated in Ref. [5].
- 205 • For the b quark charge determination the used methods are very much similar to those in 2. The
 206 vertex charge is supported by the requirements of $btag > 0.8$ and a minimal hadron momentum
 207 of 25 GeV as motivated in Ref. [6]².
- 208 • The various methods of measuring the b quark charge are also combined with the charge of the
 209 isolated lepton L . In this case an additional cut on $\gamma_t^{had} > 1.23$ is applied.
- 210 • The final decision on the t quark charge is obtained from the sum of the charges associated to
 211 the different methods. If the sum is smaller (greater) than zero then the hadronically decaying
 212 t quark candidate is said to be the t quark (\bar{t} quark).

213 Table 3 gives the final selection efficiency for the case $e_L^- e_R^+ \rightarrow t\bar{t}$ after the inclusion of the respective
 214 cuts. Table 4 shows the efficiencies after application of the various methods described in the list of items
 215 above. The addition of methods other than L_{cut} increases the efficiency by around 38%. Figure 11
 216 shows for completeness the purity of the selection for those cases in which the information from the t

¹We are aware that the set of cuts does not look straight forward and needs revision in the Post-IDR phase.

²In the $e^+e^- \rightarrow b\bar{b}$ analysis this additional requirement was removed. It would have to be investigated whether this requirement can be omitted in case of $e_L^- e_R^+ \rightarrow t\bar{t}$, too

$$e_L^- e_R^+ \rightarrow t\bar{t} \text{ at } 500 \text{ GeV}$$

General selection cuts	IDR-L	IDR-S
Isolated Lepton	92.1%	92.1%
$btag_1 > 0.8$ or $btag_2 > 0.3$	81.2%	81.1%
Thrust < 0.9	81.2%	81.1%
Hadronic mass	78.2%	78.2%
Reconstructed m_W and m_t	73.4%	73.4%
t quark polar angle spectrum		
$\gamma_t^{had.} + \gamma_t^\ell > 2.4$	62.2%	61.8%
$ p_{B,had} > 15 \text{ GeV}$	34.5%	33.9%
" $t\bar{t}$ identification"	30.6%	30.2%
b quark polar angle spectrum		
No additional cuts		

Table 3: Event selection efficiencies after pre-selection and reconstruction of the polar angle spectrum of the t quark and that of the underlying b quark.

217 quark and the \bar{t} quark decay have been combined. As in case of $e^+e^- \rightarrow b\bar{b}$ differences between the
 218 large and the small detector are observed for those combinations that include Kaons with the biggest
 219 difference for the pure Kaon combination $K + K$. The Kaon measurement is the domain of the TPC
 220 and the two models feature different outer TPC radii.

221 As a supplementary remark please note that methods available also for the fully hadronic final
 222 state yield efficiencies of 14.4% when using Methods 4-7 of Tab. 3 and 6.9% when using only Method
 223 1, respectively.

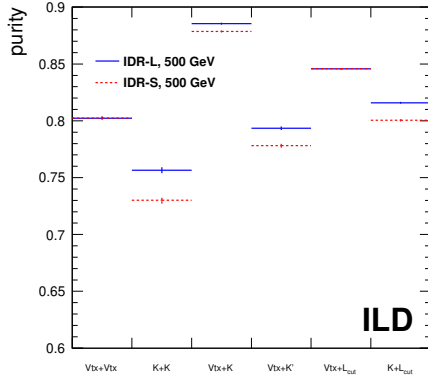


Figure 11: Purities of the various combinations to distinguish between the t and the \bar{t} quark.

Methods	IDR-L	IDR-S
1 L_{cut}	22.1%	21.9%
2 $L+Vtx$	28.6%	28.4%
3 $L+K$	29.6%	29.3%
4 $Vtx+Vtx$	30.1%	29.7%
5 $K+K$	30.3%	29.9%
6 $Vtx+K$ (same jet)	30.5%	30.1%
7 $Vtx+K$ (different jet)	30.6%	30.2%

Table 4: Efficiency increase after the progressive application of the various methods introduced to ensure a correct association of the W boson and the b quark in case of $e_L^- e_R^+ \rightarrow t\bar{t}$. The last line of this table corresponds to the line " $t\bar{t}$ identification" in Tab. 3.

$$e_R^- e_L^+ \rightarrow t\bar{t} \text{ at } 500 \text{ GeV}$$

General selection cuts	IDR-L	IDR-S
Isolated Lepton	94.1%	94.0%
$btag_1 > 0.8$ or $btag_2 > 0.3$	84.9%	84.8%
Thrust < 0.9	84.9%	84.8%
Hadronic mass	82.2%	82.3%
Reconstructed m_W and m_t	77.6%	77.5%
t quark polar angle spectrum		
$\gamma_t^{had.} + \gamma_t^\ell > 2.4$	64.1%	64.1%
b quark polar angle spectrum		
$Vtx+Vtx$	10.8%	10.3%

Table 5: See Tab. 3 for details.

224 Table 5 shows the selection efficiencies for the case $e_R^- e_L^+ \rightarrow t\bar{t}$. The cut scenario for the reconstruction
 225 of the polar angle of the t quark is much simpler than in case of $e_L^- e_R^+ \rightarrow t\bar{t}$. The reason is that
 226 the t quark direction is in first approach given by the W boson such that a wrong association of W
 227 boson and b quark doesn't alter the t quark direction. For the polar angle spectrum of the underlying
 228 b quark the analysis is restricted to the the combination of the vertex charge. This is further discussed
 229 in Sec. 5.

230 **5. Results**

231 Figure 12 shows the spectrum of the polar angle $\cos \theta_b$ after the selection given in Tabs. 1 and 2 and
 232 the application of Eq. 3 for $e_L^- e_R^+ \rightarrow b\bar{b}$. Large and small detector agree within statistical uncertainties.
 233 It seems however that there is larger migration for the small detector.

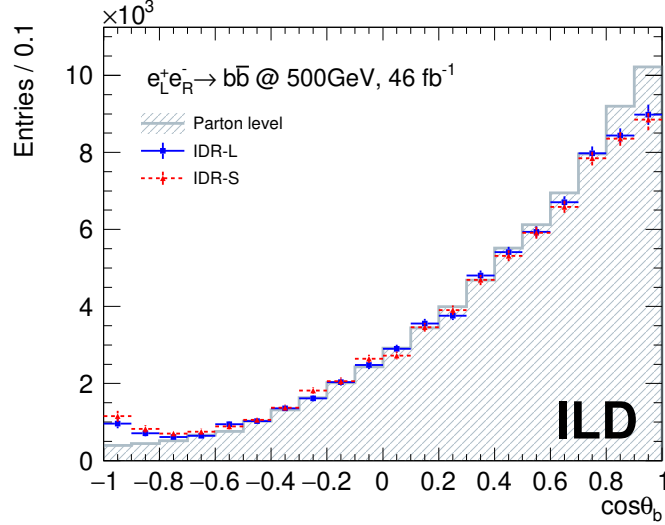


Figure 12: Polar angle spectrum for $e_L^- e_R^+ \rightarrow b\bar{b}$ at $\sqrt{s} = 500 \text{ GeV}$ after correction for acceptance and migrations due to charge mismeasurement, see Eq. 3, for the two ILD Detector models.

234 The left part of Fig. 13 shows the polar angle distribution of $t\bar{t}$ of the generated and reconstructed
 235 data for the large and the small detector models. For this all cuts and methods given in Tabs. 3
 236 and 4 have been applied. Overlaid and here and in the following figures, mainly to guide the eye,
 237 is a polynomial of second degree motivated by the approximate $d\sigma/d\cos\theta_t \sim S\cos^2\theta_t + A\cos\theta_t$
 238 dependence of the differential cross section. The right part shows the polar angle distribution of the
 239 underlying b quark for the same set of cuts. The polar spectrum can be accurately reconstructed over
 240 the entire polar angle. Acceptance drops at large absolute values of the polar angle become visible in
 241 the polar angle spectrum of the b quark (In this case no attempt was made to correct for acceptance
 242 as in Fig. 12). However, in the range $-0.8 < \cos\theta_b < 0.8$ also the polar angle of the b quark can be
 243 accurately reconstructed.

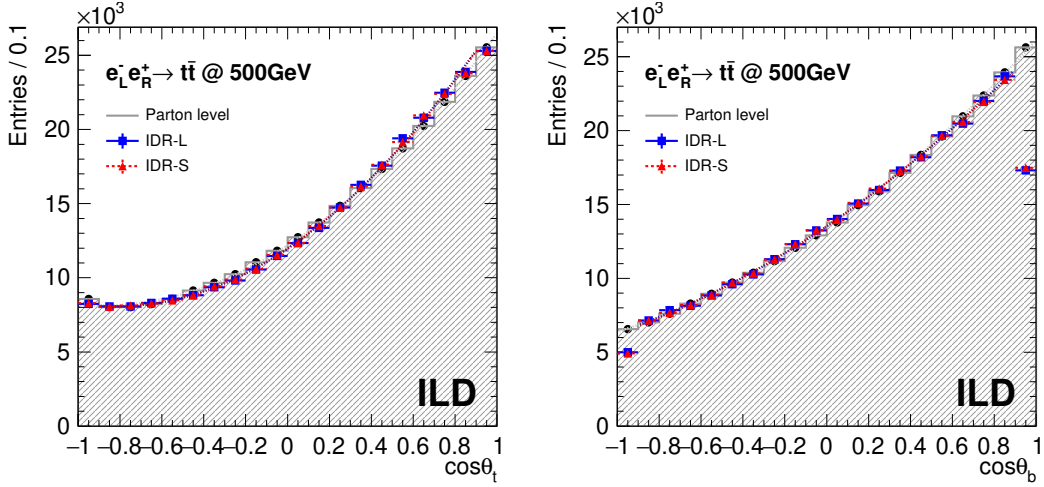


Figure 13: Results for $e_L^- e_R^+ \rightarrow t\bar{t}$ at $\sqrt{s} = 500$ GeV for the two ILD Detector models. *Left:* Polar angle distribution for t quark. *Right:* Polar angle distribution for the b quark that is issue of the t quark decay. The distributions for IDR-S is normalised to the one for IDR-L so that both histograms will be on the same level. For details on the selection, see text and Tabs. 3 and 4.

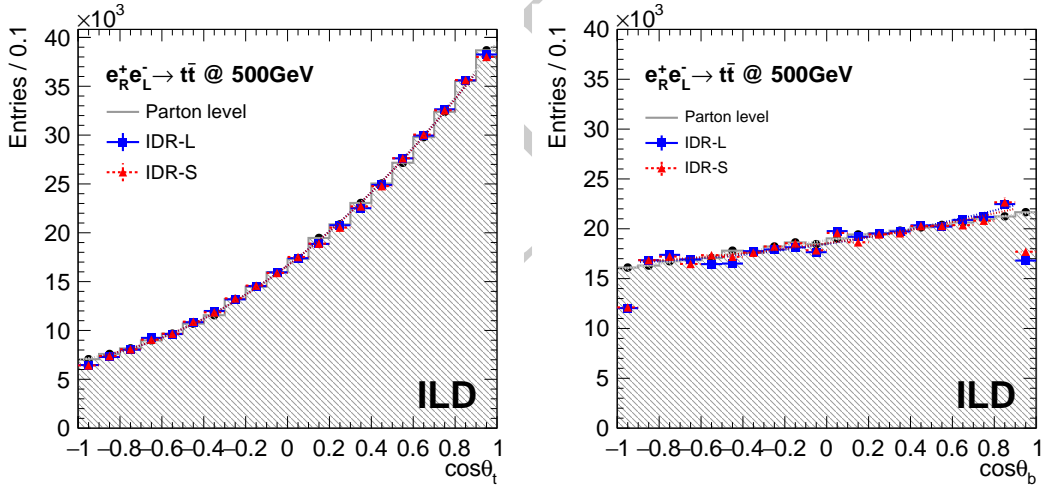


Figure 14: Same as Fig. 13 for $e_R^- e_L^+ \rightarrow t\bar{t}$. For details on the selection, see text and Tab. 5.

244 The left part of Fig. 14 shows the polar angle spectrum for the case $e_R^- e_L^+ \rightarrow t\bar{t}$ after application of
 245 the cuts introduced in Tab. 5. The generated spectrum can be very precisely reconstructed. The right
 246 hand part of Fig. 14 shows the polar angle spectrum of the underlying b quark. Here only events with
 247 consistent vertex-charge measurements have been included. The polar angle of the b quark can also
 248 in this case be very well reconstructed. However, the efficiency drops to 10% as already quantified in
 249 the lower part of Tab. 5. The inclusion of the other methods is subject to further studies. Preliminary
 250 results show that taking into account the isolated lepton “swamps” the polar angle spectrum with
 251 events in which the b quark direction is not constrained. One reason is certainly that in the case of
 252 $e_R^- e_L^+ \rightarrow t\bar{t}$ the b quark is on average softer than in the case of $e_L^- e_R^+ \rightarrow t\bar{t}$.

253 Comparing the spectra of the underlying b quarks demonstrates more clearly than the actual t quark
 254 polar angle spectra the different polarisations of the t quarks projected out by the flight direction of

255 the b quark. In case of $e_L^- e_R^+ \rightarrow t\bar{t}$ the final state is enriched with left-handed t quarks. In this case the
 256 b quark is preferably emitted in the direction of the t quark. Therefore the two polar angle spectra in
 257 Fig. 13 look similar to each other. In case of $e_R^- e_L^+ \rightarrow t\bar{t}$ the final state is enriched with right-handed
 258 t quarks. In this case the b quark is preferably emitted opposite to the direction of the t -quark. The
 259 polar angle of the b quark is a consequence of the Jacobian peak in the vicinity of $\cos\theta_{Wb} = 0$, with
 260 $\cos\theta_{Wb}$ being the opening angle between the b quark and the W boson, generated by the boost of
 261 the back-to-back configuration in the centre-of-mass frame of the decaying t quark into the laboratory
 262 frame.

263 5.1. Interpretation of the results

264 Table 6 lists the generated and reconstructed value of the forward-backward asymmetry $A_{FB, reco}^t$
 265 as an estimator for the quality of the reconstruction.

	$e_L^- e_R^+ \rightarrow t\bar{t}$		$e_R^- e_L^+ \rightarrow t\bar{t}$	
	IDR-L	IDR-S	IDR-L	IDR-S
$A_{FB, gen}^t$	0.329		0.430	
$A_{FB, reco}^t$	0.342	0.340	0.430	0.430

Table 6: Selection efficiencies and resulting $A_{FB, reco}^t$ for both beam polarisations and the two detector models under study.

266 So far the results have been presented for full beam polarisation. Using the known formula [11]

$$\sigma_{\mathcal{P}_{e^-}, \mathcal{P}_{e^+}} = \frac{1}{4} [(1 - \mathcal{P}_{e^-} \mathcal{P}_{e^+})(\sigma_{-,+} + \sigma_{+,-}) + (\mathcal{P}_{e^-} - \mathcal{P}_{e^+})(\sigma_{+,-} - \sigma_{-,+})], \quad (5)$$

267 with $\sigma_{-,+}$ and $\sigma_{+,-}$ being the fully polarised cross-sections, the results can be extrapolated to the
 268 realistic beam polarisations of $\mathcal{P}_{e^-}, \mathcal{P}_{e^+} = \mp 0.8, \pm 0.3$. The resulting Born level cross sections are
 269 1070 fb in case of $\mathcal{P}_{e^-}, \mathcal{P}_{e^+} = -0.8, +0.3$ and 519 fb in case of $\mathcal{P}_{e^-}, \mathcal{P}_{e^+} = +0.8, -0.3$. The resulting
 270 statistical errors for an integrated luminosity of $\mathcal{L} = 1600 \text{ fb}^{-1}$ at each of the two polarisation settings
 271 are given in Table 7.

	$\mathcal{P}_{e^-}, \mathcal{P}_{e^+}$	$(\delta\sigma/\sigma)_{stat.} [\%]$	$(\delta A_{FB}^t/A_{FB}^t)_{stat.} [\%]$
IDR-L	-0.8, +0.3	0.17	0.7
	+0.8, -0.3	0.25	0.53
IDR-S	-0.8, +0.3	0.17	0.7
	+0.8, -0.3	0.25	0.53

Table 7: Statistical precisions expected for the cross sections and A_{FB}^t for the case $\mathcal{P}_{e^-}, \mathcal{P}_{e^+} = -0.8, +0.3$ and the two detector models under study.

272 For both, the cross section and the forward backward asymmetry it can be expected that even at
 273 full luminosity the statistical error has to be taken into account. However, the systematic errors need
 274 to be carefully estimated. For the present analysis it would have to be checked how much the sample
 275 is contaminated by events for which the semi-leptonic decay yields τ -leptons or the τ -leptons are taken
 276 into account as in [5]. The contamination by fully hadronic $t\bar{t}$ events can be expected to be small.

277 To put the results into context, the precisions on the cross-sections and the forward-backward
 278 asymmetries are translated into precisions on electromagnetic form factors of the t quark. Figure 15
 279 shows the precisions at the 1σ level expected at ILC500. The precisions are compared with those
 280 expected after the full HL-LHC running and estimations produced for FCC-ee [12] at the same confi-
 281 dence level. For ILC500, the two sets F_1 and F_2 have been extracted separately but within each set
 282 the uncertainties have been extracted simultaneously. The projections for HL-LHC are derived from

283 the *individual* constraints of EFT Wilson coefficients presented in Tab.C2.3 of Ref. [13] (the most
 284 favorable scenario for HL-LHC). These figures demonstrate clearly the superiority of a linear e^+e^-
 285 collider with polarised beams operated at an adequate centre-of-mass energy.

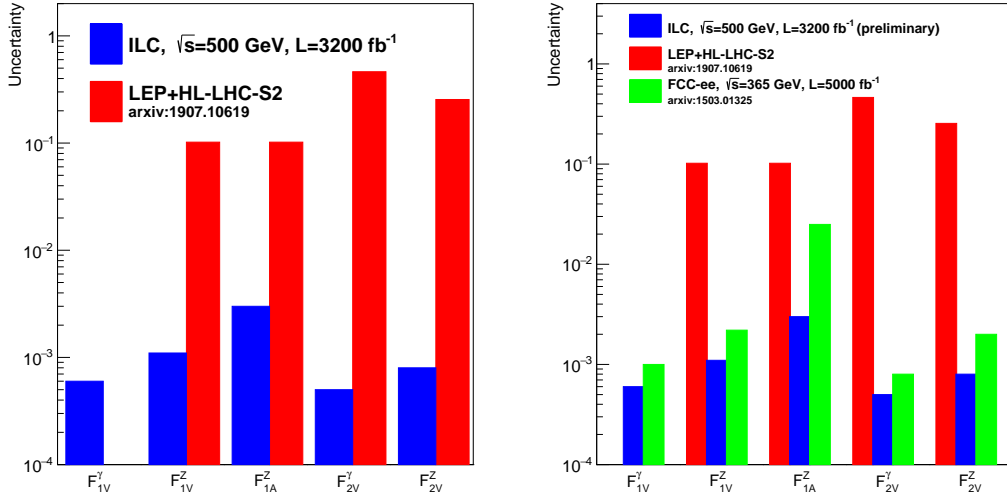


Figure 15: Precisions the on electromagnetic t quark form factors expected after ILC500 compared with those expected after the full HL-LHC running and an estimation for FCC-ee after 5000 fb^{-1} . The EFT does not include operators that map onto the F_{1V}^Y form factor. See text for further details.

286 6. Summary

287 This note presents a study of the processes $e^+e^- \rightarrow t\bar{t}$ and $e^+e^- \rightarrow b\bar{b}$ with polarised beams at
 288 $\sqrt{s} = 500$ GeV. The events are simulated and reconstructed with the large and the small models of the
 289 ILD detector.

290 In case of t quark pair production the analysis focuses on the semi-leptonic decay channel in which
 291 the isolated lepton is available for the distinction between the t quark and the \bar{t} quark. In case of
 292 the $e^+e^- \rightarrow b\bar{b}$ process the distinction has to be made by the measurement of the b quark charge,
 293 which helps also for a proper reconstruction of the $t\bar{t}$ quark pair. The charge of the b quark can be
 294 reconstructed with a purity of 80% using the combination of information available from the vertex
 295 charge, Kaons that have been measured in the TPC of ILD or isolated leptons in case of t -quark
 296 production.

297 The analysis shows that both, the large and the small detector model, are capable to provide
 298 a high precision measurement of the cross-section and the polar angle spectrum of semi-leptonic $t\bar{t}$
 299 events with a mild advantage for the large detector. Assuming a total intergrated luminosity of
 300 $\mathcal{L} = 3200 \text{ fb}^{-1}$ shared equally between the beam polarisations $\mathcal{P}_{e^-}, \mathcal{P}_{e^+} = \mp 0.8, \pm 0.3$, the cross sections
 301 of $t\bar{t}$ production can be measured to a statistical precision of about 0.2% and the forward backward
 302 asymmetry to a statistical precision of around 0.6%. The statistical precision on the cross section and
 303 the forward backward asymmetries are compatible with the scaling of the results found in [5].

304 For the first time the polar angle spectrum of the underlying b quark, issue of the t quark decay,
 305 is presented. This spectrum reveals more clearly the acceptance drop towards large polar angles. Still
 306 the polar angle of the b quark can be reconstructed accurately within $|\cos\theta| < 0.8$ for the two studied
 307 beam polarisations $\mathcal{P}_{e^-}, \mathcal{P}_{e^+} = \pm 1, \mp 1$. In case $\mathcal{P}_{e^-}, \mathcal{P}_{e^+} = +1, -1$ the efficiency drops however to
 308 10% (compared with 30% for the case $\mathcal{P}_{e^-}, \mathcal{P}_{e^+} = +1, -1$). since only the vertex charge is used for
 309 this measurement. Here further work is clearly needed to improve the event yield. Both results allow

310 however already now for the perspective that in the future the fully hadronic final state can be taken
311 into account for the analysis and that observables specific to the produced b quark can be addressed.

312 The study of the $t\bar{t}$ production has been accompanied by the second benchmark study $e^+e^- \rightarrow b\bar{b}$.
313 Since only 46 fb^{-1} are available for this channel it should be rather considered as an auxiliary study.
314 However, it is shown that the polar angle spectrum can be very well reconstructed even for the hard b
315 jets and that migrations can be controlled at a satisfactory level. It is therefore justified to conclude
316 that ILD should be able to make precision measurements in this channel even at a centre-of-mass
317 energy of 500 GeV. Although the results are similar for both the small and the large detector model,
318 this analysis, more than the analysis of the $t\bar{t}$ process reveals a slight preference for the large model.
319 This is most clearly visible in the purity of the charge measurement using Kaons, which may depend
320 on the actual TPC radius.

321 Also in the future all heavy quark studies should be carried out in close cooperation with each
322 other. As can be seen from the present study there are many common issues between the studies.
323 In the future emphasis will be put on systematic uncertainties given e.g. by hemisphere correlations.
324 These studies may be more involved in case of $t\bar{t}$ since in general the two b quarks are not back-to-back.

325 Acknowledgements

326 References

- 327 [1] F. Richard, “Present and future constraints on top EW couplings”, LAL-ORSAY-14-55, [arXiv:1403.2893](#)
328 [\[hep-ph\]](#).
- 329 [2] L. Randall and R. Sundrum, “A Large mass hierarchy from a small extra dimension”, *Phys.Rev.Lett.* **83** (1999)
330 [3370–3373](#), MIT-CTP-2860, PUPT-1860, BUHEP-99-9, [arXiv:hep-ph/9905221](#) [\[hep-ph\]](#).
- 331 [3] A. Djouadi, G. Moreau, and F. Richard, “Resolving the A(FB)**b puzzle in an extra dimensional model with an
332 extended gauge structure”, *Nucl.Phys.* **B773** (2007) 43–64, LPT-ORSAY-06-060, LAL-ORSAY-06-144,
333 [arXiv:hep-ph/0610173](#) [\[hep-ph\]](#).
- 334 [4] G. Durieux and O. Matsedonskyi, “The top-quark window on compositeness at future lepton colliders”, *JHEP* **01**
335 (2019) 072, DESY 18-114, DESY-18-114, [arXiv:1807.10273](#) [\[hep-ph\]](#).
- 336 [5] M. S. Amjad *et al.*, “A precise characterisation of the top quark electro-weak vertices at the ILC”, *Eur. Phys. J.*
337 **C75** (2015) no. 10, 512, IFIC-15-15, LAL-15-111, [arXiv:1505.06020](#) [\[hep-ex\]](#).
- 338 [6] S. Bilokin, R. Pöschl, and F. Richard, “Measurement of b quark EW couplings at ILC”, LAL-17-052,
339 [arXiv:1709.04289](#) [\[hep-ex\]](#).
- 340 [7] S. Bilokin, *Hadronic showers in a highly granular silicon-tungsten calorimeter and production of bottom and top*
341 *quarks at the ILC*. Theses, Paris Saclay, July, 2017. <https://tel.archives-ouvertes.fr/tel-01826535>.
- 342 [8] T. Behnke, J. E. Brau, P. N. Burrows, J. Fuster, M. Peskin, *et al.*, “The International Linear Collider Technical
343 Design Report - Volume 4: Detectors”, ILC-REPORT-2013-040, ANL-HEP-TR-13-20, BNL-100603-2013-IR,
344 IRFU-13-59, CERN-ATS-2013-037, COCKCROFT-13-10, CLNS-13-2085, DESY-13-062, FERMILAB-TM-2554,
345 IHEP-AC-ILC-2013-001, INFN-13-04-LNF, JAI-2013-001, JINR-E9-2013-35, JLAB-R-2013-01,
346 KEK-REPORT-2013-1, KNU-CHEP-ILC-2013-1, LLNL-TR-635539, SLAC-R-1004,
347 ILC-HIGRADE-REPORT-2013-003, [arXiv:1306.6329](#) [\[physics.ins-det\]](#). %%CITATION =
348 ARXIV:1306.6329;%%.
- 349 [9] C. Adolphsen, M. Barone, B. Barish, K. Buesser, P. Burrows, J. Carwardine, J. Clark, H. Mainaud Durand,
350 G. Dugan, E. Elsen, *et al.*, “The International Linear Collider Technical Design Report - Volume 3.II: Accelerator
351 Baseline Design”, ILC-REPORT-2013-040, ANL-HEP-TR-13-20, BNL-100603-2013-IR, IRFU-13-59,
352 CERN-ATS-2013-037, COCKCROFT-13-10, CLNS-13-2085, DESY-13-062, FERMILAB-TM-2554,
353 IHEP-AC-ILC-2013-001, INFN-13-04-LNF, JAI-2013-001, JINR-E9-2013-35, JLAB-R-2013-01,
354 KEK-REPORT-2013-1, KNU-CHEP-ILC-2013-1, LLNL-TR-635539, SLAC-R-1004,
355 ILC-HIGRADE-REPORT-2013-003, [arXiv:1306.6328](#) [\[physics.acc-ph\]](#).
- 356 [10] T. Barklow, J. Brau, K. Fujii, J. Gao, J. List, N. Walker, and K. Yokoya, “ILC Operating Scenarios”,
357 ILC-NOTE-2015-068, DESY-15-102, IHEP-AC-2015-002, KEK-PREPRINT –2015-17, SLAC-PUB-16309,
358 [arXiv:1506.07830](#) [\[hep-ex\]](#).

- 359 [11] G. Moortgat-Pick, T. Abe, G. Alexander, B. Ananthanarayan, A. Babich, *et al.*, “The Role of polarized positrons
 360 and electrons in revealing fundamental interactions at the linear collider”, *Phys.Rept.* **460** (2008) 131–243,
 361 CERN-PH-TH-2005-036, DCPT-04-100, DESY-05-059, FERMILAB-PUB-05-060-T, IPPP-04-50, KEK-2005-16,
 362 PRL-TH-05-01, SHEP-05-03, SLAC-PUB-11087, [arXiv:hep-ph/0507011](#) [hep-ph].
- 363 [12] P. Janot, “Top-quark electroweak couplings at the FCC-ee”, *JHEP* **04** (2015) 182, [arXiv:1503.01325](#) [hep-ph].
- 364 [13] G. Durieux, A. Irlles, V. Miralles, A. Peñuelas, R. Pöschl, M. Perelló, and M. Vos, “The electro-weak couplings of
 365 the top and bottom quarks – global fit and future prospects”, [arXiv:1907.10619](#) [hep-ph].

366 A. Details on particle separation via dE/dx

367 In Fig. 8.6 of the IDR the separation power between different particle types is given. A useful
 368 supplementary information of this summary is the relative frequency of the different particle types.
 369 The Fig. 16 displays the normalised dE/dx spectrum for different particles in different momentum
 370 ranges for the large and the small detector model. In both cases there is a clear separation of Kaons
 371 from pions. The latter are however much more abundant. There is only a small population of protons.
 372 Figure 17 shows the dE/dx spectra for the two processes under study.

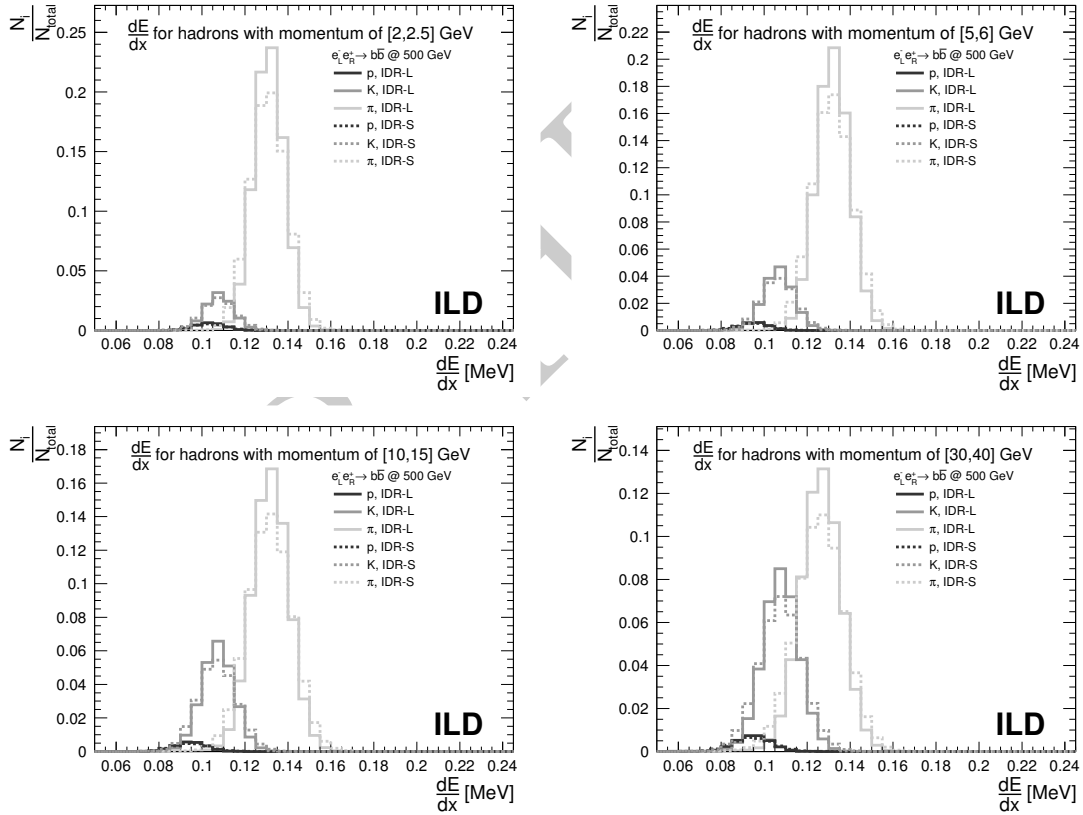


Figure 16: Projection of dE/dx for several momentum ranges. Comparison of hadron separation performance by different detector models in $b\bar{b}$ final states.

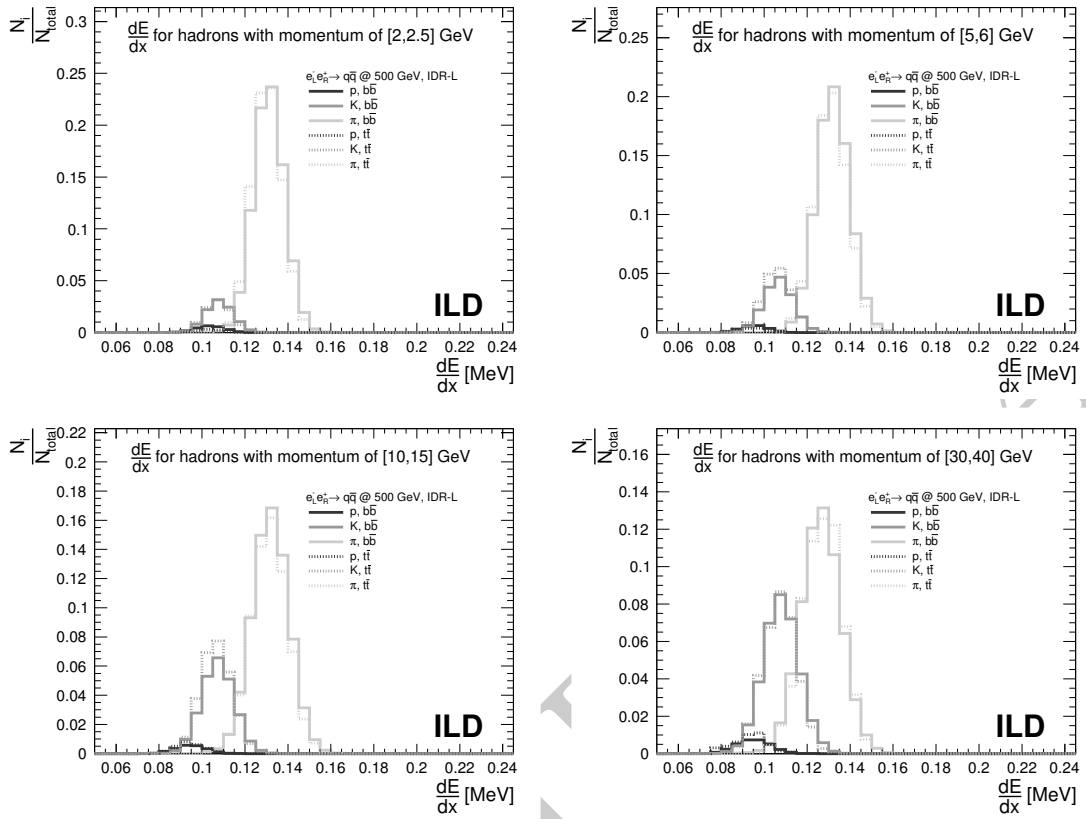


Figure 17: Projection of dE/dx for several momentum ranges. Comparison of hadron separation performance by the large model for different topologies.